


## First-principles study on the superconductivity of doped zirconium diborides

Sanjay Nayak<sup>1,\*</sup>, Chandan K. Singh,<sup>2</sup> Martin Dahlqvist,<sup>3</sup> Johanna Rosen,<sup>3</sup> Per Eklund,<sup>1</sup> and Jens Birch<sup>1</sup>

<sup>1</sup>*Thin Film Physics Division, Department of Physics, Chemistry and Biology (IFM), Linköping University, SE-581 83 Linköping, Sweden*

<sup>2</sup>*Department of Physics, Indian Institute of Science Education and Research, Pune 411008, India*

<sup>3</sup>*Materials Design Division, Department of Physics, Chemistry and Biology (IFM), Linköping University, SE-581 83 Linköping, Sweden*

 (Received 21 October 2021; revised 17 February 2022; accepted 5 April 2022; published 22 April 2022)

Recent experiments [Barbero *et al.* *Phys. Rev. B* **95**, 094505 (2017)] have established that bulk superconductivity ( $T_c \sim 8.3\text{--}8.7$  K) can be induced in  $\text{AlB}_2$ -type  $\text{ZrB}_2$  and  $\text{HfB}_2$ , highly covalent refractory ceramics, by vanadium (V) doping. These  $\text{AlB}_2$ -structured phases provide an alternative to earlier diamondlike or diamond-based superconducting and superhard materials. However, the underlying mechanism for doping-induced superconductivity in these materials is yet to be addressed. In this paper, we have used first-principles calculations to probe electronic structure, lattice dynamics, and electron-phonon coupling (EPC) in V-doped  $\text{ZrB}_2$  and consequently examine the origin of the superconductivity. We find that, while doping-induced stress weakens the EPC, the concurrently induced charges strengthen it. The calculated critical transition temperature ( $T_c$ ) in electron (and V)-doped  $\text{ZrB}_2$  is at least one order of magnitude lower than experiments, despite considering the weakest possible Coulomb repulsion between electrons in the Cooper pair, hinting a complex origin of superconductivity in it.

DOI: [10.1103/PhysRevMaterials.6.044805](https://doi.org/10.1103/PhysRevMaterials.6.044805)

### I. INTRODUCTION

Transition metal diborides ( $\text{TMB}_2$ ) in  $\text{AlB}_2$ -type crystal structure (space group:  $P6/mmm$  [191]) are hard and ultrahigh-temperature ceramic materials [1–5] and have applications in, e.g., cutting tools, crucibles, wear-resistant coatings, and microelectronics [6–9]. The mechanical hardness, e.g., Vickers hardness ( $H_v$ ), of  $\text{TMB}_2$  varies from  $\sim 12\text{--}15$  GPa to  $\sim 45\text{--}50$  GPa. Particularly in thin film form, the group-4 diborides such as  $\text{TiB}_2$  [10,11],  $\text{ZrB}_2$  [12,13], and  $\text{HfB}_2$  [14,15] are superhard with the measured indentation hardness of  $\approx 45$ ,  $\approx 45$ , and  $\approx 43$  GPa, respectively. While the measured hardnesses of group-5 borides (i.e.,  $\text{VB}_2$  [1],  $\text{NbB}_2$  [16], and  $\text{TaB}_2$  [5]) are in the range of  $\sim 30$  to  $\sim 40$  GPa, the indentation hardness of group-6 borides (i.e.,  $\text{CrB}_2$  [17,18],  $\text{MoB}_2$  [19,20], and  $\text{WB}_2$  [21]) is within 30 GPa.  $\text{TMB}_2$  in their pristine and stoichiometric  $\text{AlB}_2$ -type phase are typically not superconductors [22–26], but suitable doping conditions can induce superconductivity [25,27–29]. For example,  $\text{ZrB}_2$  and  $\text{HfB}_2$  are metals in their pristine form, but upon doping with V, they become superconducting with a critical transition temperature ( $T_c$ )  $< 10$  K [27,29].

Similarly, Ni-doped  $\text{NbB}_2$  becomes superconducting  $< 6$  K [28]. Along with their high hardness mechanical properties, doping-induced superconductivity in these  $\text{TMB}_2$  make them a commercially cheap alternative to nanocomposites that contain diamond and/or c-BN. Superconducting, superhard nanocomposites are important for industrial application in high-pressure cryogenic devices [30,31], wear-resistant parts of superconducting devices, superconducting micro-electro mechanical systems [32], superconducting radiofrequency accelerator cavities [33–35], quantum interference devices [36], photodetectors [37], infrared sensors [38], and electrical contacts to nanodevices [39]. Despite the numerous studies to explain the origin of superconductivity in  $\text{MgB}_2$  with  $\text{AlB}_2$ -type structure [40–43], little is known about the doped  $\text{TMB}_2$  family of materials [23]. Consequently, from both perspectives of applications and fundamental material science, there is a need to understand the superconductivity in these doped  $\text{TMB}_2$  phases. In view of that, we chose V-doped  $\text{ZrB}_2$  as a representative member since it has the highest  $T_c$  reported for this family of materials.

In its pristine form,  $\text{ZrB}_2$  is not superconducting, but doping with V or Nb as low as 1% can induce superconductivity [27,29,44,45]. Renosto *et al.* [29] reported that the highest  $T_c$  recorded for  $\text{Zr}_{1-x}\text{V}_x\text{B}_2$  is 8.7 K for  $x = 0.04$ . Along with the multigap nature of the superconducting gap ( $2\Delta$ ), they demonstrated that  $T_c$  increases with increasing V content in  $\text{Zr}_{1-x}\text{V}_x\text{B}_2$  up to  $x = 0.04$  and that further increase in V-doping levels causes  $T_c$  to decrease, which implies the presence of a superconducting dome. From x-ray diffraction analysis, a dopant concentration of 4% V in  $\text{ZrB}_2$  results in a uniaxial compressive strain of  $\sim 0.3\%$  along the

\*sanjay.kumar.nayak@liu.se

Published by the American Physical Society under the terms of the [Creative Commons Attribution 4.0 International license](https://creativecommons.org/licenses/by/4.0/). Further distribution of this work must maintain attribution to the author(s) and the published article's title, journal citation, and DOI. Funded by [Bibsam](https://www.bibsam.org/).

$c$  axis. Using microscopic characterization techniques such as nuclear magnetic resonance, superconducting quantum interference device magnetometry, resistivity, and muon-spin rotation measurements, Barbero *et al.* [27] established the bulk superconductivity ( $T_c = 8.33$  K) in  $\text{Zr}_{0.96}\text{V}_{0.04}\text{B}_2$  along with an  $s$ -wave and the multigap nature of  $2\Delta$ , which was further validated by Jung *et al.* [46].

In this paper, we investigate the electronic structure, lattice dynamics, and electron-phonon coupling (EPC) in pristine and V-doped  $\text{ZrB}_2$  using first-principles simulation to explore the origin of the superconductivity with  $<4\%$  doping level. Our analysis reveals that, upon V doping, the Fermi level ( $E_F$ ) shifts toward the conduction band, making V an effectively  $n$ -type dopant to  $\text{ZrB}_2$ . This shifting of  $E_F$  away from the well-known pseudogap region in the electronic structure of ceramics enhances the electronic densities of states (DOSs) at  $E_F$ ,  $[N(E_F)]$ , and improves the EPC. However, at experimentally relevant doping levels, our calculated superconducting transition temperature ( $T_c$ ) is one order of magnitude lower than the reported experimental values, an indication for a complex origin of superconductivity in V-doped  $\text{ZrB}_2$ .

## II. COMPUTATIONAL DETAILS

Our analysis involves uncovering the effects of (i) lattice strain, (ii) carrier doping, and (iii) alloying within virtual crystal approximations (VCAs) of the electronic, vibrational, and their coupling in  $\text{ZrB}_2$  using first-principles density functional theory simulations as implemented in the QUANTUM ESPRESSO code [47]. Nonrelativistic norm-conserving pseudopotentials with the Perdew-Burke-Ernzerhof exchange-correlation functional are used in our simulations [48,49]. The valence electronic configuration of Zr, V, and B are chosen as  $4s^2 4p^6 5s^2 4d^2$ ,  $3s^2 3p^6 4s^2 3d^3$ , and  $2s^2 2p^1$ , respectively. For ground state calculations, the Brillouin zone is sampled by a grid of  $14 \times 14 \times 13$  k-points [50], and a kinetic energy cutoff for the plane-wave basis of  $\approx 1090$  eV is used. Dynamical matrices are computed over a  $6 \times 6 \times 6$  q-points grid using density functional perturbation theory. EPC was computed with the Wannier interpolated scheme [51]; 13 maximally localized Wannier functions [52,53] are constructed using the WANNIER90 library [54] within the EPW code [51]. Further details are given in Sec. I in the Supplemental Material [55]. The electron-phonon matrix elements are calculated on dense k- and q-grids of  $25 \times 25 \times 25$ . We have used 300 and 0.5 meV as electron and phonon smearing widths, respectively. Within the Migdal-Eliashberg theory [56,57], the isotropic version of Eliashberg spectral function  $\alpha^2 F(\omega)$  is defined as

$$\alpha^2 F(\omega) = \frac{1}{N(E_F)} \sum_{mny} \int \frac{d\mathbf{k}}{\Omega_{\text{BZ}}} \int \frac{d\mathbf{q}}{\Omega_{\text{BZ}}} |g_{mny}(\mathbf{k}, \mathbf{q})|^2 \times \delta(\varepsilon_{n\mathbf{k}} - \varepsilon_F) \delta(\varepsilon_{m\mathbf{k}+\mathbf{q}} - \varepsilon_F) \delta(\omega - \omega_{\mathbf{q}\gamma}), \quad (1)$$

where  $N(E_F)$  is the electronic DOS at the Fermi level and  $g_{mny}(\mathbf{k}, \mathbf{q})$  are the electron-phonon matrix elements with electronic band indices  $m, n$  and phonon band index  $\gamma$ . The  $\sum_{mny} \int \frac{d\mathbf{k}}{\Omega_{\text{BZ}}} \delta(\varepsilon_{n\mathbf{k}} - \varepsilon_F) \delta(\varepsilon_{m\mathbf{k}+\mathbf{q}} - \varepsilon_F)$  term of Eq. (1) is referred to nesting function ( $\zeta_q$ ) and is a property of the Fermi surface and hence has a pure electronic origin [51]. After com-

puting  $\alpha^2 F(\omega)$ , electron-phonon interaction  $\lambda$  is evaluated by

$$\lambda = 2 \int_0^\infty \frac{\alpha^2 F(\omega)}{\omega} d\omega. \quad (2)$$

The superconducting transition temperature  $T_c$  is calculated by the McMillan-Allen-Dynes formula [58,59]:

$$T_c = \frac{\omega_{\text{log}}}{1.2} \exp \left[ -\frac{1.04(1 + \lambda)}{\lambda - \mu^*(1 + 0.62\lambda)} \right], \quad (3)$$

where  $\omega_{\text{log}}$  is a logarithmically averaged phonon frequency which has replaced the Debye temperature  $\Theta_D$  in the McMillan formula and is computed from  $\alpha^2 F(\omega)$  as

$$\omega_{\text{log}} = \exp \left[ \frac{2}{\lambda} \int_0^\infty \log \omega \frac{\alpha^2 F(\omega)}{\omega} d\omega \right]. \quad (4)$$

In Eq. (3),  $\mu^*$  is a dimensionless parameter representing the Coulomb repulsion between electrons which form the Cooper pair. This repulsive parameter is hard to compute from the *ab initio* method, and for most superconductors, its value lies in the range 0.1–0.2 [60–62]. However, for  $d$ -band metals, Bennemann and Garland [63] approximated  $\mu^*$  to  $N(E_F)$  as

$$\mu^* = 0.26 \times \frac{N(E_F)}{1 + N(E_F)}. \quad (5)$$

Our estimates of  $\mu^*$  for doped  $\text{ZrB}_2$  are in the range of 0.05–0.09 with a doping level of 0.0 to 0.2  $e^-/\text{cell}$ . Nevertheless, we estimate  $T_c$  for a wide range (0.0–0.1) of  $\mu^*$  in this paper. To model the V doping in  $\text{ZrB}_2$ , VCA is used where the Zr atomic site in  $\text{ZrB}_2$  is replaced with a virtual atom. The pseudopotential of the virtual atom is, in turn, represented by a composition average of the Zr and V pseudopotentials, i.e.,  $V_{\text{virtual atom}}^x = xV_V + (1-x)V_{\text{Zr}}$ , and the atomic mass of the virtual atom is taken as the average atomic mass of Zr and V, i.e.,  $m_{\text{virtual atom}} = xm_V + (1-x)m_{\text{Zr}}$ .

## III. RESULTS AND DISCUSSION

Our optimized lattice parameters  $a = b = 3.17 \text{ \AA}$  and  $c = 3.54 \text{ \AA}$  for a unit cell (u.c.) of  $\text{ZrB}_2$  as well as in-plane B-B bond length ( $d_{B-B} = 1.83 \text{ \AA}$ ) and out-of-plane Zr-B ( $d_{\text{Zr-B}} = 2.55 \text{ \AA}$ ) are in good agreement with previous theory and experiments [64–66]. The electronic band structure of pristine  $\text{ZrB}_2$  shows a Dirac-like linear band dispersion along the  $M$ - $K$ ,  $K$ - $\Gamma$ , and  $\Gamma$ - $A$  high-symmetry k-path [see Fig. 1(a)]. The linear dispersed band along the  $M$ - $K$  symmetry line is  $\sim 2$  eV, which is rarely observed in Dirac materials. The features in the band structure match with previously reported ones [67,68]. The orbital projected electronic DOS shows a dominant role of the Zr-4d orbital toward the conduction bands, while a B-2p orbital is more dominant at valence bands along with a contribution from a Zr-4d orbital [see Fig. 1(b)], again in good agreement with a previous report [69]. The Fermi level ( $E_F$ ) is located near a pseudogap region of the electronic DOS [Fig. 1(b)], resulting in a relatively low  $N(E_F)$  [ $= 0.26$  states  $\text{eV}^{-1} \text{cell}^{-1}$ ], smaller than the  $N(E_F)$  of  $\text{MgB}_2$  [ $= 0.72$  states  $\text{eV}^{-1} \text{cell}^{-1}$ ] [70].

The unit cell of  $\text{ZrB}_2$  consists of three atoms which results in a total of nine phonon branches, three acoustic and six

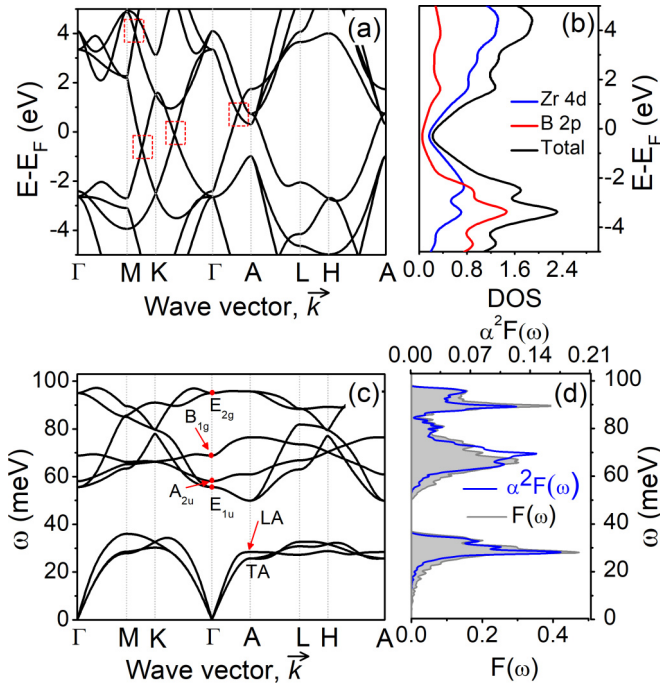


FIG. 1. (a) Electronic band structure and (b) density of states (DOS) of pristine AIB<sub>2</sub>-type ZrB<sub>2</sub>. Red rectangles in (a) mark Dirac-like bands. (c) Phonon dispersion and (d) phonon DOS [ $F(\omega)$ ]. The isotropic Eliashberg spectral functions [ $\alpha^2F(\omega)$ ] are overlaid in (d).

optical ( $2E_{1u} + 1A_{2u} + 1B_{1g} + 2E_{2g}$ ), as shown in Fig. 1(c). The  $\Gamma$ -point phonon frequencies of  $E_{1u}$ ,  $A_{2u}$ ,  $B_{1g}$ , and  $E_{2g}$  optical modes are found at 55.61, 58.08, 68.79, and 95.02 meV, respectively [see Fig. 1(c) and Table I]. The phonon DOSs [ $F(\omega)$ ] and the isotropic Eliashberg spectral functions [ $\alpha^2F(\omega)$ ] are displayed in Fig. 1(d), which shows that spectral patterns of  $\alpha^2F(\omega)$  replicate  $F(\omega)$ . Using Eq. (2), we estimate the average value of the EPC constant ( $\lambda$ ) to 0.126, in agreement with previous theoretical and experimental reports [71–73]. It is noted here that, unlike in MgB<sub>2</sub>, the  $E_{2g}$  phonon in ZrB<sub>2</sub> is at higher energy than the  $B_{1g}$  one at the  $\Gamma$  point. Thus, the contribution of  $E_{2g}$  phonon modes to the  $\alpha^2F(\omega)$  of ZrB<sub>2</sub> is weaker than that of MgB<sub>2</sub> [74]. Together with low  $N(E_F)$ , energetics of  $E_{2g}$  phonon modes in vibrational

TABLE I. Computed  $\Gamma$ -point phonon frequencies of optical phonons at various doping levels. Frequencies corresponding to  $Zr_{1-x}V_xB_2$  are obtained within VCA.

Configuration	Doping level (e <sup>-</sup> /cell)	Phonon frequency (meV)			
		$E_{1u}$	$A_{2u}$	$B_{1g}$	$E_{2g}$
ZrB <sub>2</sub>	0.0	55.61	58.08	68.79	95.02
	0.037	55.55	57.96	68.46	94.45
	0.1	55.38	57.79	67.36	92.76
	0.125	55.30	57.72	66.89	92.76
	0.15	55.21	57.66	66.47	92.33
	0.2	55.02	57.52	65.88	91.75
Zr <sub>0.963</sub> V <sub>0.037</sub> B <sub>2</sub>	–	56.08	58.49	68.61	95.33
Zr <sub>0.875</sub> V <sub>0.125</sub> B <sub>2</sub>	–	57.12	59.37	67.46	95.56

spectra are responsible for a weaker EPC strength in ZrB<sub>2</sub> than MgB<sub>2</sub>. This weaker EPC is the primary cause of absence of superconductivity in ZrB<sub>2</sub>. The Debye temperature ( $\Theta_D$ ) is estimated to be 560 K, in agreement with the experimental value of 555.6 K by Renosto *et al.* [29]. For details, see Sec. II in the Supplemental Material [55]. The facts that the experimental  $n$ -type carrier density in ZrB<sub>2</sub> of the order of  $10^{21}$  electrons cm<sup>-3</sup> [67] is consistent with the carrier densities considered in our simulations and that the  $E_F \gg \Theta_D$  condition is satisfied suggest that the Eliashberg formalism is adequate to describe the electron-phonon interaction and consequently the superconductivity in ZrB<sub>2</sub> [75]. The weak EPC in pristine ZrB<sub>2</sub> ( $\lambda = 0.126$ ) results in a superconducting temperature in the mK range. With the Coulomb repulsion constant  $\mu^* = [0, 0.1]$ , the upper limit of the transition temperature  $T_c$  using the McMillan-Allen-Dynes equation is  $<0.04$  K (Fig. S8 in the Supplemental Material [55]), which explains the absence of the superconductivity  $>1$  K in pristine ZrB<sub>2</sub> [76].

The electronic structure of V-doped ZrB<sub>2</sub> is investigated using both supercell and VCA approaches. In the supercell approach, we considered two different supercells (i)  $2 \times 2 \times 2$  (24 atoms) and (ii)  $3 \times 3 \times 3$  (81 atoms) and substituted one V atom for Zr, resulting in a V-doping concentration of 12.5% (Zr<sub>0.875</sub>V<sub>0.125</sub>B<sub>2</sub>) and 3.7% (Zr<sub>0.963</sub>V<sub>0.037</sub>B<sub>2</sub>), respectively. Upon V doping in ZrB<sub>2</sub>, the  $E_F$  moves away from the pseudogap region into the conduction band [Fig. 2(a)], resulting in increased  $N(E_F)$ . The calculated  $N(E_F)$  for Zr<sub>0.963</sub>V<sub>0.037</sub>B<sub>2</sub> and Zr<sub>0.875</sub>V<sub>0.125</sub>B<sub>2</sub> are 0.34 and 0.52 states eV<sup>-1</sup>cell<sup>-1</sup>, respectively. The atom projected DOS for Zr<sub>0.963</sub>V<sub>0.037</sub>B<sub>2</sub> shows that V-3d states are more localized than Zr-4d states near the Fermi level [Figs. 2(b)–2(c)], with a major contribution from  $d_{z^2}$ . We also note the splitting of degenerate Zr- $d_{xz}$  and  $d_{yz}$  orbitals upon V doping in ZrB<sub>2</sub>. Band structure analysis by Zhai *et al.* [23] further suggests that  $E_F$  of Zr<sub>0.963</sub>V<sub>0.037</sub>B<sub>2</sub> is very close to the  $d_{xy} + d_{yz}$  band at the A high-symmetry k-point with a low dispersion width.

Full structural relaxation for supercells of Zr<sub>0.963</sub>V<sub>0.037</sub>B<sub>2</sub> and Zr<sub>0.875</sub>V<sub>0.125</sub>B<sub>2</sub> shows compressive strain along both in-plane and out-of-plane directions as compared with ZrB<sub>2</sub>. While the change in volume ( $\Delta V/V_0$ ), in-plane ( $\Delta a/a_0$ ), and out-of-plane ( $\Delta c/c_0$ ) lattice parameters of Zr<sub>0.963</sub>V<sub>0.037</sub>B<sub>2</sub> are  $-0.80$ ,  $-0.23$ , and  $-0.35\%$ , the same for Zr<sub>0.875</sub>V<sub>0.125</sub>B<sub>2</sub> are  $-2.67$ ,  $-0.72$ , and  $-1.25\%$ , respectively.

Similar numbers are obtained when using VCA, with optimized lattice parameters  $a$  ( $c$ ) of Zr<sub>0.963</sub>V<sub>0.037</sub>B<sub>2</sub> and Zr<sub>0.875</sub>V<sub>0.125</sub>B<sub>2</sub> being 3.16 Å (3.52 Å) and 3.15 Å (3.48 Å), respectively. This corresponds to in-plane (out-of-plane) compressive strain of  $-0.31\%$  ( $-0.56\%$ ) and  $-0.63$  ( $-1.7\%$ ), respectively, as compared with pristine ZrB<sub>2</sub>. The larger compressive strain out-of-plane as compared with in-plane agrees qualitatively well with the experimental observations where strain along the  $c$  axis is well resolved, while almost no in-plane strain is noted [29]. The electronic band structure and DOS analysis revealed that the  $E_F$  moves away from the pseudogap region into the conduction band with a corresponding increase in  $N(E_F)$  for V-doped ZrB<sub>2</sub> (see Sec. VI in the Supplemental Material [55]). Using VCA,  $N(E_F)$  of Zr<sub>0.963</sub>V<sub>0.037</sub>B<sub>2</sub> and Zr<sub>0.875</sub>V<sub>0.125</sub>B<sub>2</sub> are 0.32 and 0.46 states eV<sup>-1</sup>cell<sup>-1</sup>, respectively. Comparison of the electronic structure calculated at 4% of V doping



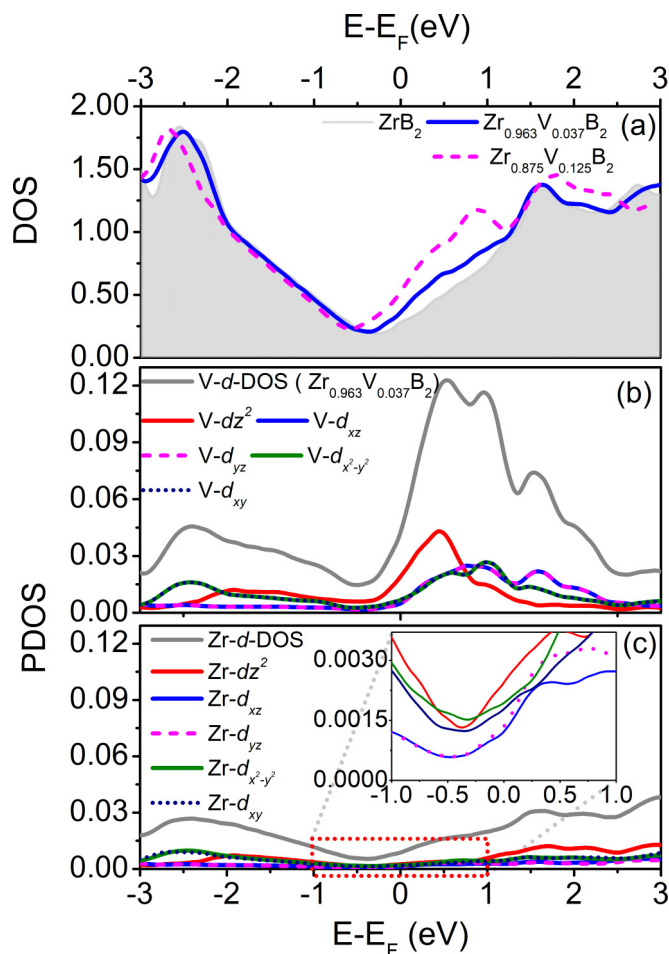


FIG. 2. (a) Electronic density of states (DOS) per unit cell of V-doped  $\text{ZrB}_2$  obtained with two different supercell dimensions:  $3 \times 3 \times 3$  for  $\text{Zr}_{0.963}\text{V}_{0.037}\text{B}_2$  (blue solid line) and  $2 \times 2 \times 2$  for  $\text{Zr}_{0.875}\text{V}_{0.125}\text{B}_2$  (magenta dashed line). (b) Atom and (c) orbital projected DOS of V and Zr atoms in  $\text{Zr}_{0.963}\text{V}_{0.037}\text{B}_2$ . The inset in (c) shows orbital-projected Zr states around the Fermi level ( $E_F$ ).

using the supercell approach and VCA reveals similar results, while at 12.5% of doping levels,  $N(E_F)$  from VCA calculations [ $N(E_F)^{\text{VCA}} = 0.46$  states  $\text{eV}^{-1}\text{cell}^{-1}$ ] is significantly lower than achieved with the supercell approach [ $N(E_F)^{\text{SC}} = 0.52$  states  $\text{eV}^{-1}\text{cell}^{-1}$ ].

Although at macroscopic scale the strain is relatively low ( $-0.23$  to  $-0.35\%$ ), our bond-length distribution analysis from supercell approach ( $\text{Zr}_{0.963}\text{V}_{0.037}\text{B}_2$ ) calculations revealed that the maximum change in bond lengths of Zr-B in the supercell is as high as  $-1.9\%$ . Thus, we examine the material properties of  $\text{ZrB}_2$  over a wide range of uniaxial compressive strain ( $\varepsilon_{\parallel c}$ ), e.g., 0.3, 0.5, 1, 3, and 5%. The electronic band structure revealed that the bands at the  $A$  symmetry k-point are becoming closer to  $E_F$  upon compressive stress, and at  $\varepsilon_{\parallel c} = 5\%$ , a new Fermi pocket appears at the  $A$  point of the Brillouin zone (see Sec. III in the Supplementary Material [55] for band structure, DOS, and Fermi surface plot). We do not find any substantial changes in  $N(E_F)$  upon uniaxial compressive strain along the  $c$  axis.

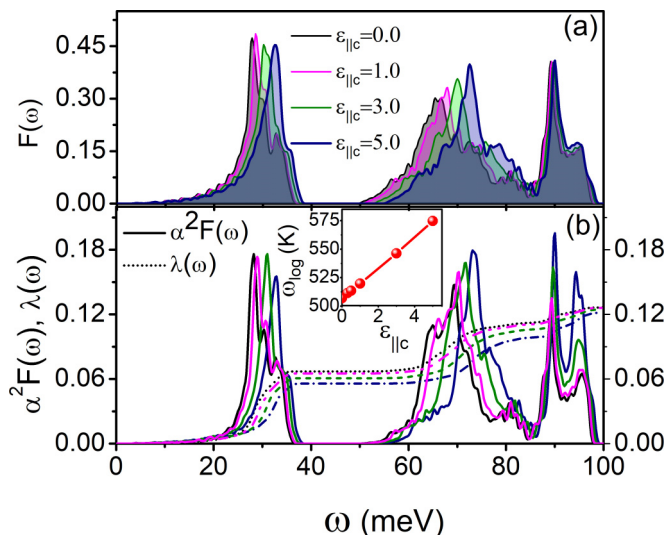


FIG. 3. (a) Phonon density of states (DOS) [ $F(\omega)$ ] of uniaxially strained ( $\varepsilon_{\parallel c}$ )  $\text{ZrB}_2$  with different strains in unit cell configurations. (b) The isotropic Eliashberg spectral function [ $\alpha^2 F(\omega)$ , solid lines] and electron-phonon coupling constant [ $\lambda(\omega)$ , dashed lines] of strained  $\text{ZrB}_2$ . Inset in (b): Logarithmic average of phonon frequencies ( $\omega_{\log}$ ) in units of Kelvin as a function of applied strain.

Phonon band and  $F(\omega)$  analysis reveals that, upon compressive strain, phonon frequencies shift toward higher energy, known as phonon hardening, as seen in Figs. 3(a) and S7 in the Supplementary Material [55]), and hence, no imaginary modes of vibrations are observed even if the strain ( $\varepsilon_{\parallel c}$ ) is relatively high ( $=5\%$ ). Recent theoretical results suggest that a thin film of layered borides like  $\text{MgB}_4$  and  $\text{InB}_4$  will go for structural phase transition with a relatively smaller biaxial compressive strain of  $-0.8$  and  $3\%$ , respectively [77,78]. Similarly, layered  $\text{AlB}_2$  can maintain structural stability from only  $-1.5\%$  (compressive) to  $7.5\%$  (tensile) strain [79,80], suggesting that bulk  $\text{ZrB}_2$  is structurally more stable to compressive stress than the mentioned layered structure of borides.

We further notice that, while the dispersion width of acoustic phonons is increasing, optical phonons are becoming flatter, i.e., increase in  $F(\omega)$ , upon compressive strain. The effect of phonon hardening is further reflected in the spectral intensity of  $\alpha^2 F(\omega)$  and consequently in  $\lambda$  and  $\omega_{\log}$ . The estimated  $\lambda$  of  $\text{ZrB}_2$  with  $\varepsilon_{\parallel c} = 0.3, 0.5, 1, 3,$  and  $5\%$  are 0.125, 0.125, 0.125, 0.124, and 0.121, respectively, which indicates a lowering of the average EPC upon uniaxial compressive strain. Upon compressive strain, the  $\lambda$  contribution from acoustic phonons ( $\lambda_{\text{aco.}}$ ) is reduced, while the component of optical phonons ( $\lambda_{\text{opt.}}$ ) is enhanced [see Fig. 3(b)]. The change in  $\omega_{\log}$  is linear with applied uniaxial compressive strain [see inset of Fig. 3(b)] and is estimated to be 506.8, 511.4, 513.4, 519.7, 546.3, and 574.7 K for  $\varepsilon_{\parallel c} = 0.0, 0.3, 0.5, 1, 3,$  and  $5\%$ , respectively. The computed  $T_c$  using Eq. (3) is lower than for the pristine  $\text{ZrB}_2$  ( $<0.04$  K) when  $\mu^* = [0, 0.1]$  (see Fig. S8 in the Supplementary Material [55]). This indicates that doping-induced compressive strain is not responsible for the superconductivity in V-doped  $\text{ZrB}_2$ . The effect of uniaxial compressive strain on vibrational properties and  $T_c$  of  $\text{ZrB}_2$

is opposite to that of monolayer  $\text{AlB}_2$  and multilayered layered  $\text{InB}_4$ , where phonon softening and increases in  $T_c$  are estimated [77–79].

Next, we examine the effect of electron doping of  $\text{ZrB}_2$ . It is noteworthy that the highest value of  $T_c$  is observed for 4% doping of V/Nb [29], where each V or Nb atom donates one electron per atom for the conduction. This corresponds to a doping of 0.04 electrons per primitive unit cell. However, to reveal trends and clarify, the electronic and vibrational properties were computed self-consistently for a range of charge doping levels ( $n$ ), i.e., 0.037, 0.1, 0.125, 0.15, 0.2, and 0.4 electrons/cell, leading to an electron doping concentration of  $1.2 \times 10^{21}$  to  $1.2 \times 10^{22} \text{cm}^{-3}$  in  $\text{ZrB}_2$ . A compensating jellium background is used to neutralize the charge in the cell. In this paper, we simulate electron doping for two different cases: (i) full relaxation of both structural parameters and ions and (ii) only relaxation of ions while keeping the unit cell static. In the former case, we find an expansion of the unit cell lattice upon carrier doping, contrary to experimental observations; hence, we present the results from case (ii). Details of case (i) are discussed in Sec. VII in the Supplemental Material [55].

Electron doping of  $\text{ZrB}_2$  results in  $E_F$  moving away from the pseudogap region and into the conduction band (see Fig. S12(A) in the Supplemental Material [55]), causing an increase in  $N(E_F)$ , as shown in Fig. 4(e). At a carrier doping of  $0.1 e^-/\text{cell}$ ,  $E_F$  is close to the  $d_{xz}/d_{yz}$  bands at the  $A$  point in the similar condition to the supercell calculation of  $\text{Zr}_{0.963}\text{V}_{0.037}\text{B}_2$  [44]. This is shown in Fig. S11 in the Supplemental Material [55]. Analysis of phonon bands and  $F(\omega)$  in Figs. 4(a) and S13 in the Supplemental Material [55] shows both acoustic and optical phonon modes shift toward lower energy, henceforth referred to as phonon softening, upon electron doping in  $\text{ZrB}_2$ . The  $\Gamma$ -point phonon frequencies of optical phonon modes with different doping concentrations are tabulated in Table I and quantify the phonon softening at the  $\Gamma$ -point for electron-doped  $\text{ZrB}_2$ .

With increased doping levels comes phonon softening which, in turn, leads to increased overall spectral weightage of  $\alpha^2F(\omega)$ . The spectral weight of lower frequency transverse acoustic (TA-1) phonons increases up to a doping level of  $0.1 e^-/\text{cell}$  and remains constant afterwards, while contribution from high-frequency transverse acoustic (TA-2) and longitudinal acoustic (LA) modes increase continuously with increase in doping levels [see inset of Fig. 4(b)]. It is important to note here that a small but noticeable difference in  $\alpha^2F(\omega)$  is observed between two different lattice relaxation methods (see Figs. 4(b) and S14 in the Supplemental Material [55]). While contribution from acoustic phonons to  $\alpha^2F(\omega)$  is fixed after a doping level of  $0.1 e^-/\text{cell}$ , the contribution of optical phonons to  $\alpha^2F(\omega)$  steadily increases with the doping level increment [see Fig. 4(b)].

The enhancement in  $\lambda$  is almost linear with the doping level, and it increased from 0.126 to 0.240 with an increase in the doping level from 0.0 to  $0.2 e^-/\text{cell}$  [see Fig. 4(c)]. Even though the phonon softening causes enhancement in  $\lambda$ , it has a detrimental effect on  $\omega_{\log}$ , which is lowered with increased doping levels [see Fig. 4(d)]. The quantitative difference in estimated  $\lambda$  and  $\omega_{\log}$  with two different lattice relaxed configurations is clearly visible in Figs. 4(c) and 4(d). This

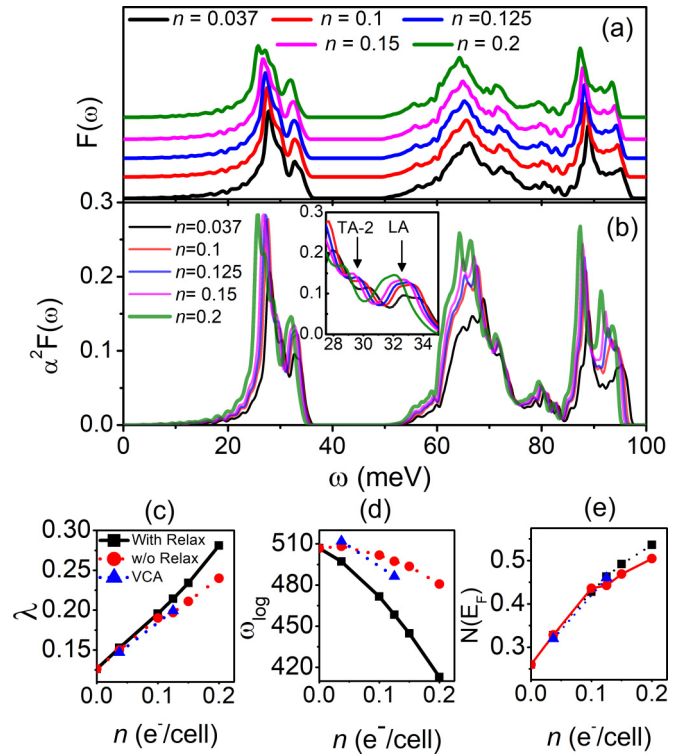


FIG. 4. (a) Phonon density of states (DOS) [ $F(\omega)$ ] of electron-doped  $\text{ZrB}_2$  with different electron-doping concentrations ( $n$  in units of  $e^-/\text{cell}$ ). (b) The isotropic Eliashberg spectral function [ $\alpha^2F(\omega)$ ] for various electron-doped levels considered in this paper. Inset of figure (b) is enlarged version of  $\alpha^2F(\omega)$  as a function of high acoustic phonon energies. Note that both (a) and (b) are obtained for the configuration at which only ionic degrees of freedom were allowed (see text for details). (c)–(e) Electron-phonon coupling constant ( $\lambda$ ), logarithmic average of phonon frequencies ( $\omega_{\log}$ ), and electronic DOS at the Fermi level [ $N(E_F)$ ] as a function of doping concentrations, respectively. For virtual crystal approximation (VCA),  $n$  represents the V-doping concentration ( $x$ ) in  $\text{Zr}_{1-x}\text{V}_x\text{B}_2$ .

can be attributed to a larger amplitude in phonon softening when the system is allowed for complete relaxation of both lattice parameters and ions (see Fig. S13 in the Supplemental Material [55]).

The phonon softening in electron-doped  $\text{ZrB}_2$  is obvious. However, the results from VCA are slightly different. We find phonon hardening in  $\text{Zr}_{0.963}\text{V}_{0.037}\text{B}_2$  and  $\text{Zr}_{0.875}\text{V}_{0.125}\text{B}_2$  as compared with  $\text{ZrB}_2$ . The only exception is a small phonon softening of  $B_{1g}$  phonons within VCA (see Table I and Sec. VI in the Supplemental Material [55]). Despite overall phonon hardening, we find an increase in spectral weight of  $\alpha^2F(\omega)$  in  $\text{Zr}_{0.963}\text{V}_{0.037}\text{B}_2$  and  $\text{Zr}_{0.875}\text{V}_{0.125}\text{B}_2$ . This indicates that the electron states at the Fermi level  $N(E_F)$  dictate EPC in doped  $\text{ZrB}_2$ . To explain the enhancement in electron-phonon interaction and phonon softening for electron-doped  $\text{ZrB}_2$ , we have calculated the Fermi nesting function  $\zeta_q$  [see Fig. 5]. The nesting function  $\zeta_q$  is the imaginary part of electronic susceptibility, responsible for the Fermi surface topology and one of the major terms in the Migdal-Eliashberg picture of electron-phonon interaction. By Eqs. (1) and (2), the increment in the nesting function can enhance the electron-phonon

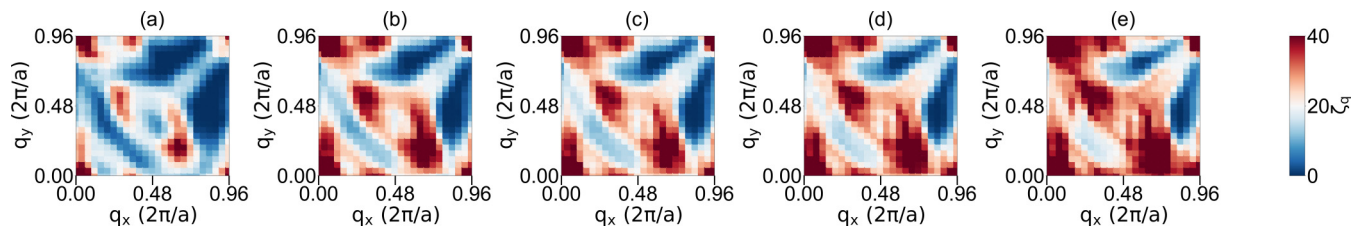


FIG. 5. (a)–(e)  $q_x$ - $q_y$  projected nesting function ( $\zeta_q$ ) computed over the irreducible wedge of the Brillouin zone of doped ZrB<sub>2</sub> with doping levels of 0.037, 0.1, 0.125, 0.15, and 0.2  $e^-$ /cell, respectively. Clearly, an enhancement in  $\zeta_q$  with increase in doping levels is observed.

interaction, and this argument is supported by reported calculations [81,82] on electron-phonon interaction.

The nesting function is one of the reasons behind the softening of the phonon modes and can be responsible for the charge density wave state [83–85]. Further, the Fermi nesting function is associated with the imaginary part of electronic susceptibility [86,87], closely related to the Fermi surface topology [88], and strongly influences the electron-phonon interactions [89]. With an increase in doping levels, we observed the appearance of electron-type Fermi pockets around the  $A$  points with the overall Fermi surface becoming broader (see Fig. S12(B) in the Supplemental Material [55]). It indicates that the Fermi surface topology has changed with electron doping, which also reflects in the broader peak in the Fermi nesting function [see Fig. 5]. In the electron-doped ZrB<sub>2</sub> case, the enhanced nesting function  $\zeta_q$  further explains the phonon softening at higher doping. The estimated  $\lambda$  values for Zr<sub>0.963</sub>V<sub>0.037</sub>B<sub>2</sub> and Zr<sub>0.875</sub>V<sub>0.125</sub>B<sub>2</sub> are 0.147 and 0.199, which are close to 0.150 (0.037  $e^-$ /cell) and 0.197 (0.125  $e^-$ /cell) for electron-doped ZrB<sub>2</sub> [see Fig. 4(c)]. Similarly, computed  $\omega_{\log}$  for the same cases are 511.9 and 486.3 K within VCA, in close agreement with values of electron-doped ZrB<sub>2</sub> [see Fig. 4(d)]. We also note that, in the case where atomic configurations (i.e., cell parameters + ions) of bare electron-doped ZrB<sub>2</sub> could relax completely, a noticeable difference in  $\lambda$  and  $\omega_{\log}$  is found, particularly at higher doping levels [see Figs. 4(c) and 4(d)].

Now we calculate the superconducting transition temperature ( $T_c$ ) using Eq. (3) and also estimate  $T_c$  by solving the isotropic Eliashberg gap [ $\Delta(T)$ ] equations [60,90]. In the latter case,  $\Delta(T)$  is interpolated by the cubic-spline technique, and  $T_c$  is the temperature at which  $\Delta(T) = 0$ . We find that both methods provide similar values of  $T_c$  (see Figs. 6 and S17 and S18 in the Supplemental Material [55]). We start by analyzing  $T_c$  with lowest extreme of  $\mu^*$ . At the experimental doping level (4% of V  $\leftrightarrow$  0.037  $e^-$ /cell), the computed  $T_c(\mu^* = 0.0)$  is 0.14 K [see Fig. 6(a)]. This is much lower than the reported experimental values of 8.33 to 8.7 K. Despite an increase in the doping level to  $n = 0.2 e^-$ /cell,  $T_c$  is estimated to be 1.8 K. It is important to note that the abovementioned  $T_c$  is the maximum extreme value, with a decrease of  $T_c$  with increasing  $\mu^*$  [see Figs. 6(b) and 6(c)]. For  $\mu^* = 0.05$ , the computed  $T_c$  is in the range of 0.001 to 0.328 K with a doping level of 0.037–0.2  $e^-$ /cell. Based on these results, the calculated  $T_c$ , for equal or even higher than experimental doping levels, is at least one order of magnitude lower than experimental values despite using an extremely minimal value of  $\mu^*$ . The experimental value of  $T_c$  is obtained for

a doping level of 0.4  $e^-$ /cell [ $\approx 10^{22} \text{cm}^{-3}$ ] and  $\mu^* = 0.0$  [see Fig. 6(a)]. However, it does not appear reasonable to equate  $\mu^*$  to zero at this high doping level. Using computed  $N(E_F)$  for the doping level of 0.4  $e^-$ /cell in Eq. (5),  $\mu^*$  is estimated to be 0.11. These high values of  $\mu^*$  result in a  $T_c \approx 0.8$  K, one order of magnitude smaller than the experimental value of 8.3–8.7 K.

To find a possible explanation for this severe underestimation of  $T_c$  by the isotropic Eliashberg theory, we have calculated momentum-resolved electron-phonon interactions for various doping levels (see Fig. S19 in the Supplemental Material [55]). In all doping levels, the distribution of electron-phonon interaction has only a single peak for which spreading increases with doping. The maximally doped ZrB<sub>2</sub> has a shorter spread, reflecting its lesser anisotropic nature than MgB<sub>2</sub> [60]. Unlike MgB<sub>2</sub>, doped ZrB<sub>2</sub> does not have isolated multiple sheets of the Fermi surface and is quite small, resulting in being more isotropic with lesser electron-phonon strength. These features of doped ZrB<sub>2</sub> provides a McMillan-Allen-Dynes  $T_c$  one order lower than that of MgB<sub>2</sub> using the isotropic Eliashberg theory [60]. With more isotropic electron-phonon interaction, the nearly continuous Fermi surface and lower isotropic transition temperature indicate that the solution of the anisotropic Eliashberg equations will not result in the increase in theoretical estimation of superconducting transition temperature for doped ZrB<sub>2</sub> as they do in pristine MgB<sub>2</sub> [60,91,92]. It is important to note that V doping

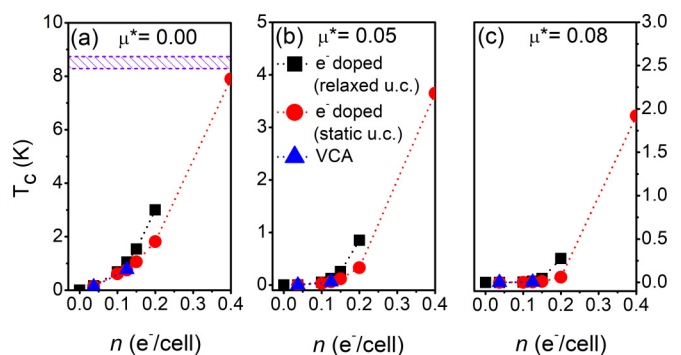


FIG. 6. Calculated superconducting transition temperature ( $T_c$ ) as a function of electron doping in a unit cell (u.c.) for three different values of effective screened Coulomb repulsion constant (a)  $\mu^* = 0.0$ , (b)  $\mu^* = 0.05$ , and (c)  $\mu^* = 0.08$  in Eq. (3). For virtual crystal approximation (VCA),  $n$  represents the V-doping concentration ( $x$ ) in Zr<sub>1-x</sub>V<sub>x</sub>B<sub>2</sub>. The shaded region in (a) indicates the range of experimentally reported values (i.e., 8.3–8.7 K).



in ZrB<sub>2</sub> creates localized *d*-band defect states near the Fermi level (see Fig. 2), which could not be completely replicated in the electronic structure of electron-doped ZrB<sub>2</sub> nor within the VCA. Often, localized defect states enhance the average EPC strength ( $\lambda$ ) in materials [93,94]. The formation of a VB<sub>2</sub>-like local region in Zr<sub>1-x</sub>V<sub>x</sub>B<sub>2</sub> may further enhance the average EPC strength as VB<sub>2</sub> has a relatively larger EPC strength ( $\lambda_{\text{VB}_2} = 0.28$ ) and almost the same logarithmic average of phonon frequencies ( $\omega_{\text{log}}$ ) as ZrB<sub>2</sub> [95,96]. Also, the effect of local inhomogeneity of V in Zr<sub>1-x</sub>V<sub>x</sub>B<sub>2</sub> cannot be completely ignored, as it can play a nontrivial role in enhancing the superconducting transition temperature as observed in Cu-doped Bi<sub>2</sub>Se<sub>3</sub> [97,98]. All these phenomena together or individually may influence the average EPC strength ( $\lambda$ ) and consequently the determination of the superconducting transition temperature ( $T_c$ ). Thus, we suggest a mechanism beyond those investigated earlier is responsible for the observed superconductivity.

Experiments suggest that superconductivity in V-doped ZrB<sub>2</sub> have bulk nature. To eliminate the role of compositional fluctuations in V-doped ZrB<sub>2</sub>, Renosto *et al.* [29] carried out temperature ( $T$ )-dependence measurements of the specific heat ( $C_p$ ) at zero applied magnetic field. A clear jump in  $C_p/T$  vs  $T^2$  is observed, which was consistent with their magnetization ( $M$ ) vs  $T$  and resistivity ( $\rho$ ) vs  $T$  measurements. Similar observations were found for Nb-doped ZrB<sub>2</sub> [44]. Both Renosto *et al.* [29] and Marques *et al.* [44] found that, at low temperature, the electronic contribution to specific heat at log scale [ $\ln(C_e/\gamma T_c)$ ] as a function of  $T_c/T$  shows a clear deviation from typical Bardeen-Cooper-Schrieffer (BCS)-type behavior. The change in  $\Delta C/\gamma T_c$  from nonsuperconducting to superconducting phase was determined to 0.42 [29] and 0.15 [44], values that are considerably smaller than the weak-coupling BCS theory value ( $\sim 1.43$ ). The superconducting gap [ $\Delta(0)$ ]-to-temperature ( $T$ ) ratio in Zr<sub>0.97</sub>V<sub>0.03</sub>B<sub>2</sub>, being  $2\Delta(0)/k_B T_c \approx 8.95$ , is much higher than the BCS theory of  $\approx 3.5$  [45]. Along with the experiments discussed above, our theoretical results hint that superconductivity in V-doped ZrB<sub>2</sub> is of complex origin.

#### IV. CONCLUSIONS

In summary, we have examined the origin of superconductivity in electron-doped AlB<sub>2</sub>-type ZrB<sub>2</sub> within Migdal-Eliashberg formalism using various approaches. We found that doping-induced uniaxial compressive strain along the *c* direction causes a weakening of the EPC owing to acoustic and low-frequency phonon hardening which suppress superconductivity. Contrary to compressive strain, electron-doping-induced carriers strengthen the EPC due to enhancement of densities of electronic states at the Fermi level as well as softening of both acoustic and optical phonons. Even though the calculated EPC constant in ZrB<sub>2</sub> is enhanced upon carrier doping, it is not sufficiently large to explain the superconducting transition temperature of 8.3–8.7 K within standard phonon-mediated superconductivity theory. The highest value of calculated superconducting temperature is one order of magnitude lower with respect to reported experimental transition temperatures, which indicates a complex origin of the superconductivity in ZrB<sub>2</sub>. The results indicate that further theoretical and experimental studies are required to understand the origin of this superconductivity. Electron doping in V-doped ZrB<sub>2</sub> can be related to a relatively localized V-4*d* orbital, whose role in the superconductivity warrants further investigation. The nontrivial topologically-like bands appearing near the Fermi level of ZrB<sub>2</sub>, which are robust upon doping, may be important for this superconductivity.

#### ACKNOWLEDGMENTS

The calculations were carried out using supercomputer resources provided by the Swedish National Infrastructure for Computing at the National Supercomputer Centre partially funded by the Swedish Research Council through Grant Agreement No. 2018-05973. The Knut and Alice Wallenberg (KAW) Foundation is acknowledged for support through the Wallenberg Academy Fellows program and Scholar program (P.E., Grant No. 2020.0196, J.R., Grants No. 2018.0146 and No. 2019.0433) and for a KAW Project grant (No. 2015.0043).

- 
- [1] V. Moraes, L. Zauner, T. Wojcik, M. Arndt, P. Polcik, H. Riedl, and P. H. Mayrhofer, *Acta Mater.* **186**, 487 (2020).
  - [2] Q. Gu, G. Krauss, and W. Steurer, *Adv. Mater.* **20**, 3620 (2008).
  - [3] B. Bakhit, D. L. J. Engberg, J. Lu, J. Rosen, H. Högborg, L. Hultman, I. Petrov, J. E. Greene, and G. Greczynski, *J. Vac. Sci. Technol. A* **37**, 031506 (2019).
  - [4] L. E. Pangilinan, C. L. Turner, G. Akopov, M. Anderson, R. Mohammadi, and R. B. Kaner, *Inorg. Chem.* **57**, 15305 (2018).
  - [5] V. Šroba, T. Fiantok, M. Truchlý, T. Roch, M. Zahoran, B. Grančič, P. Švec, Š. Nagy, V. Izai, P. Kúš, and M. Mikula, *J. Vac. Sci. Technol. A* **38**, 033408 (2020).
  - [6] P. H. Mayrhofer, A. Kirnbauer, P. Ertelthaler, and C. M. Koller, *Scr. Mater.* **149**, 93 (2018).
  - [7] W. G. Fahrenholtz and G. E. Hilmas, *Int. Mater. Rev.* **57**, 61 (2012).
  - [8] S. Jayaraman, Y. Yang, D. Y. Kim, G. S. Girolami, and J. R. Abelson, *J. Vac. Sci. Technol. A* **23**, 1619 (2005).
  - [9] R. G. Munro, *J. Res. Natl. Inst. Stand. Technol.* **105**, 709 (2000).
  - [10] M. Mikula, B. Grančič, V. Buršíková, A. Csuba, M. Držík, Š. Kavecký, A. Plecenik, and P. Kúš, *Vacuum* **82**, 278 (2007).
  - [11] P. H. Mayrhofer, C. Mitterer, J. G. Wen, J. E. Greene, and I. Petrov, *Appl. Phys. Lett.* **86**, 131909 (2005).
  - [12] L. Tengdelius, E. Broitman, J. Lu, F. Eriksson, J. Birch, T. Nyberg, L. Hultman, and H. Högborg, *Acta Mater.* **111**, 166 (2016).
  - [13] E. Broitman, L. Tengdelius, U. D. Hangen, J. Lu, L. Hultman, and H. Högborg, *Scr. Mater.* **124**, 117 (2016).
  - [14] A. Chatterjee, N. Kumar, J. R. Abelson, P. Bellon, and A. A. Polycarpou, *Wear* **265**, 921 (2008).
  - [15] A. A. Goncharov, S. N. Dub, and A. V. Agulov, *Phys. Met. Metallogr.* **114**, 95 (2013).
  - [16] N. Liu, L. Dong, S. Jin, R. Wan, H. Gu, and D. Li, *J. Alloys Compd.* **695**, 3225 (2017).

- [17] M. Audronis, A. Leyland, P. J. Kelly, and A. Matthews, *Surf. Coatings Technol.* **201**, 3970 (2006).
- [18] P. V. Kiryukhantsev-Korneev, J. F. Pierson, M. I. Petrzhik, M. Alnot, E. A. Levashov, and D. V. Shtansky, *Thin. Solid. Films* **517**, 2675 (2009).
- [19] P. Malinovskis, J. Palisaitis, P. O. Å. Persson, E. Lewin, and U. Jansson, *J. Vac. Sci. Technol. A* **34**, 031511 (2016).
- [20] Q. Tao, X. Zhao, Y. Chen, J. Li, Q. Li, Y. Ma, J. Li, T. Cui, P. Zhu, and X. Wang, *RSC Adv.* **3**, 18317 (2013).
- [21] Y. M. Liu, C. L. Jiang, Z. L. Pei, H. Lei, J. Gong, and C. Sun, *Surf. Coatings Technol.* **245**, 108 (2014).
- [22] N. I. Medvedeva, A. L. Ivanovskii, J. E. Medvedeva, and A. J. Freeman, *Phys. Rev. B* **64**, 020502 (2001).
- [23] H. Zhai, F. Munoz, and A. N. Alexandrova, *J. Mater. Chem. C* **7**, 10700 (2019).
- [24] Y. Ma, J. S. Tse, T. Cui, D. D. Klug, L. Zhang, Y. Xie, Y. Niu, and G. Zou, *Phys. Rev. B* **72**, 014306 (2005).
- [25] L. E. Muzzy, M. Avdeev, G. Lawes, M. K. Haas, H. W. Zandbergen, A. P. Ramirez, J. D. Jorgensen, and R. J. Cava, *Physica C Supercond.* **382**, 153 (2002).
- [26] M. Mudgel, V. P. S. Awana, G. L. Bhalla, and H. Kishan, *Solid State Commun.* **147**, 439 (2008).
- [27] N. Barbero, T. Shiroka, B. Delley, T. Grant, A. J. S. Machado, Z. Fisk, H. R. Ott, and J. Mesot, *Phys. Rev. B* **95**, 094505 (2017).
- [28] S. T. Renosto, R. Lang, E. Diez, L. E. Corrêa, M. S. da Luz, Z. Fisk, and A. J. S. Machado, *J. Alloys Compd.* **787**, 414 (2019).
- [29] S. T. Renosto, H. Conso-line, C. A. M. Dos Santos, J. Albino Aguiar, S. G. Jung, J. Vanacken, V. V. Moshchalkov, Z. Fisk, and A. J. S. MacHado, *Phys. Rev. B* **87**, 174502 (2013).
- [30] T. A. Prikhna, W. Gawalek, Y. A. M. Savchuk, N. V. Sergienko, V. E. Moshchil, V. Sokolovsky, J. Vajda, V. N. Tkach, F. Karau, H. Weber, M. Eisterer, A. Joulain, J. Rabier, X. Chaud, M. Wendt, J. Dellith, N. I. Danilenko, T. Habisreuther, S. N. Dub, V. Meerovich *et al.*, *Acta Phys. Pol. A* **117**, 7 (2010).
- [31] T. A. Prikhna, *Low Temp. Phys.* **32**, 505 (2006).
- [32] T. Bautze, S. Mandal, O. A. Williams, P. Rodière, T. Meunier, and C. Bäuerle, *Carbon N. Y.*, **72**, 100 (2014).
- [33] H. S. Padamsee, *Annu. Rev. Nucl. Part. Sci.* **64**, 175 (2014).
- [34] S. Posen and D. L. Hall, *Supercond. Sci. Technol.* **30**, 033004 (2017).
- [35] S. Posen, J. Lee, D. N. Seidman, A. Romanenko, B. Tennis, and O. S. Melnychuk, *Supercond. Sci. Technol.* **34**, 025007 (2021).
- [36] S. Mandal, T. Bautze, O. A. Williams, C. Naud, É. Bustarret, F. Omnes, P. Rodière, T. Meunier, C. Bäuerle, and L. Saminadayar, *ACS Nano* **5**, 7144 (2011).
- [37] P. Rath, O. Kahl, S. Ferrari, F. Sproll, G. Lewes-Malandrakis, D. Brink, K. Ilin, M. Siegel, C. Nebel, and W. Pernice, *Light Sci. Appl.* **4**, e338 (2015).
- [38] M. J. M. E. de Nivelles, M. P. Bruijn, R. de Vries, J. J. Wijnbergen, P. A. J. de Korte, S. Sánchez, M. Elwenspoek, T. Heidenblut, B. Schwierzi, W. Michalke, and E. Steinbeiss, *J. Appl. Phys.* **82**, 4719 (1997).
- [39] A. Y. Kasumov, R. Deblock, M. Kociak, B. Reulet, H. Bouchiat, I. I. Khodos, Y. B. Gorbatov, V. T. Volkov, C. Journet, and M. Burghard, *Science* **284**, 1508 (1999).
- [40] H. J. Choi, D. Roundy, H. Sun, M. L. Cohen, and S. G. Louie, *Nature (London)* **418**, 758 (2002).
- [41] J. Bekaert, A. Aperis, B. Partoens, P. M. Oppeneer, and M. V. Milošević, *Phys. Rev. B* **96**, 094510 (2017).
- [42] J. A. Alarco, P. C. Talbot, and I. D. R. Mackinnon, *Phys. C Supercond. Its Appl.* **536**, 11 (2017).
- [43] A. Floris, G. Profeta, N. N. Lathiotakis, M. Lüders, M. A. L. Marques, C. Franchini, E. K. U. Gross, A. Continenza, and S. Massidda, *Phys. Rev. Lett.* **94**, 037004 (2005).
- [44] M. D. R. Marques, F. S. Portela, L. T. Corredor, G. Zhang, J. Vanacken, V. V. Moshchalkov, L. E. Correa, S. T. Renosto, O. Cigarroa, A. J. S. MacHado, and J. A. Aguiar, *Supercond. Sci. Technol.* **29**, 095007 (2016).
- [45] R. E. López-Romero and R. Escudero, *J. Supercond. Nov. Magn.* **28**, 2953 (2015).
- [46] S. G. Jung, J. Vanacken, V. V. Moshchalkov, S. T. Renosto, C. A. M. Dos Santos, A. J. S. MacHado, Z. Fisk, and J. Albino Aguiar, *J. Appl. Phys.* **114**, 133905 (2013).
- [47] P. Giannozzi, S. Baroni, N. Bonini, M. Calandra, R. Car, C. Cavazzoni, D. Ceresoli, G. L. Chiarotti, M. Cococcioni, I. Dabo *et al.*, *J. Phys. Condens. Matter* **21**, 395502 (2009).
- [48] J. P. Perdew, K. Burke, and M. Ernzerhof, *Phys. Rev. Lett.* **77**, 3865 (1996).
- [49] D. R. Hamann, *Phys. Rev. B* **88**, 085117 (2013).
- [50] H. J. Monkhorst and J. D. Pack, *Phys. Rev. B* **13**, 5188 (1976).
- [51] S. Ponce, E. R. Margine, C. Verdi, and F. Giustino, *Comput. Phys. Commun.* **209**, 116 (2016).
- [52] N. Marzari and D. Vanderbilt, *Phys. Rev. B* **56**, 12847 (1997).
- [53] N. Marzari, A. A. Mostofi, J. R. Yates, I. Souza, and D. Vanderbilt, *Rev. Mod. Phys.* **84**, 1419 (2012).
- [54] G. Pizzi, V. Vitale, R. Arita, S. Blugel, F. Freimuth, G. Geranton, M. Gibertini, D. Gresch, C. Johnson, T. Koretsune, J. Ibanez-Azpiroz, H. Lee, J. M. Lihm, D. Marchand, A. Marrazzo, Y. Mokrousov, J. I. Mustafa, Y. Nohara, Y. Nomura, L. Paulatto *et al.*, *J. Phys. Condens. Matter* **32**, 165902 (2019).
- [55] See Supplemental Material at <http://link.aps.org/supplemental/10.1103/PhysRevMaterials.6.044805> for details about the construction of Wannier functions and electronic band structure, phonon dispersion, and superconducting gap of V-doped ZrB<sub>2</sub>.
- [56] A. B. Migdal, *Sov. Phys. JETP* **7**, 996 (1958).
- [57] G. M. Eliashberg, *Sov. Phys. JETP* **11**, 696 (1960).
- [58] P. B. Allen and R. C. Dynes, *Phys. Rev. B* **12**, 905 (1975).
- [59] W. L. McMillan, *Phys. Rev.* **167**, 331 (1968).
- [60] E. R. Margine and F. Giustino, *Phys. Rev. B* **87**, 024505 (2013).
- [61] J. M. An and W. E. Pickett, *Phys. Rev. Lett.* **86**, 4366 (2001).
- [62] M. Aslam, C. K. Singh, S. Das, R. Kumar, S. Datta, S. Halder, S. Gayen, M. Kabir, and G. Sheet, *J. Phys. Condens. Matter* **30**, 255002 (2018).
- [63] K. H. Bennemann and J. W. Garland, *AIP Conf. Proc.* **4**, 103 (1972).
- [64] H. Fu, M. Teng, X. Hong, Y. Lu, and T. Gao, *Phys. B Condens. Matter* **405**, 846 (2010).
- [65] F. Ling, L. Hao, K. Luo, Z. Yuan, Y. Gao, Q. Gao, Y. Li, Z. Zhao, Y. Zhang, and D. Yu, *Comput. Mater. Sci.* **176**, 109517 (2020).
- [66] W. G. Fahrenholtz, G. E. Hilmas, I. G. Talmy, and J. A. Zaykoski, *J. Am. Ceram. Soc.* **90**, 1347 (2007).
- [67] R. Lou, P. Guo, M. Li, Q. Wang, Z. Liu, S. Sun, C. Li, X. Wu, Z. Wang, Z. Sun, D. Shen, Y. Huang, K. Liu, Z. Y. Lu, H. Lei, H. Ding, and S. Wang, *npj Quantum Mater.* **3**, 43 (2018).
- [68] X. Feng, C. Yue, Z. Song, Q. Wu, and B. Wen, *Phys. Rev. Materials* **2**, 014202 (2018).



- [69] M. Dahlqvist, U. Jansson, and J. Rosen, *J. Phys. Condens. Matter* **27**, 435702 (2015).
- [70] J. Kortus, I. I. Mazin, K. D. Belashchenko, V. P. Antropov, and L. L. Boyer, *Phys. Rev. Lett.* **86**, 4656 (2001).
- [71] P. P. Singh, *Phys. Rev. B* **69**, 094519 (2004).
- [72] S. M. Sichkar, V. N. Antonov, and V. P. Antropov, *Phys. Rev. B* **87**, 064305 (2013).
- [73] G. Fuchs, S.-L. Drechsler, K.-H. Müller, A. Handstein, S. V. Shulga, G. Behr, A. Gümbel, J. Eckert, K. Nenkov, V. N. Narozhnyi *et al.*, *J. Low Temp. Phys.* **131**, 1159 (2003).
- [74] H. J. Choi, M. L. Cohen, and S. G. Louie, *Phys. C Supercond.* **385**, 66 (2003).
- [75] M. Meinert, *Phys. Rev. Lett.* **116**, 137001 (2016).
- [76] V. A. Gasparov, N. S. Sidorov, and I. I. Zver'Kova, *Phys. Rev. B* **73**, 094510 (2006).
- [77] Z. Wang, S. Zeng, Y. Zhao, X. Wang, and J. Ni, *Phys. Rev. B* **104**, 174519 (2021).
- [78] Y. Zhao, C. Lian, S. Zeng, Z. Dai, S. Meng, and J. Ni, *Phys. Rev. B* **101**, 104507 (2020).
- [79] Y. Zhao, C. Lian, S. Zeng, Z. Dai, S. Meng, and J. Ni, *Phys. Rev. B* **100**, 094516 (2019).
- [80] J. Bekaert, M. Petrov, A. Aperis, P. M. Oppeneer, and M. V. Milošević, *Phys. Rev. Lett.* **123**, 077001 (2019).
- [81] A. V. Lugovskoi, M. I. Katsnelson, and A. N. Rudenko, *Phys. Rev. B* **99**, 064513 (2019).
- [82] T. Bazhurov, J. Noffsinger, and M. L. Cohen, *Phys. Rev. B* **82**, 184509 (2010).
- [83] F. Clerc, C. Battaglia, M. Bovet, L. Despont, C. Monney, H. Cercellier, M. G. Garnier, P. Aebi, H. Berger, and L. Forró, *Phys. Rev. B* **74**, 155114 (2006).
- [84] M. I. Katsnelson, I. I. Naumov, and A. V. Trefilov, *Phase Transitions* **49**, 143 (1994).
- [85] A. Landa, P. Söderlind, I. I. Naumov, J. E. Klepeis, and L. Vitos, *Computation* **6**, 29 (2018).
- [86] M. D. Johannes, I. I. Mazin, and C. A. Howells, *Phys. Rev. B* **73**, 205102 (2006).
- [87] M. D. Johannes and I. I. Mazin, *Phys. Rev. B* **77**, 165135 (2008).
- [88] M. Sunagawa, T. Ishiga, K. Tsubota, T. Jabuchi, J. Sonoyama, K. Iba, K. Kudo, M. Nohara, K. Ono, H. Kumigashira *et al.*, *Sci. Rep.* **4**, 7330 (2014).
- [89] K. Terashima, Y. Sekiba, J. H. Bowen, K. Nakayama, T. Kawahara, T. Sato, P. Richard, Y.-M. Xu, L. J. Li, G. H. Cao *et al.*, *Proc. Natl. Acad. Sci. USA* **106**, 7330 (2009).
- [90] G. A. C. Umharino, in *Emergent Phenomena in Correlated Matter*, edited by E. Pavarini, E. Koch, and U. Schollwöck (Forschungszentrum Jülich, Jülich, 2013), Chap. 13.
- [91] C. Heil, S. Poncé, H. Lambert, M. Schlipf, E. R. Margine, and F. Giustino, *Phys. Rev. Lett.* **119**, 087003 (2017).
- [92] F. Giustino, *Rev. Mod. Phys.* **89**, 015003 (2017).
- [93] R. Atta-Fynn, P. Biswas, and D. A. Drabold, *Phys. Rev. B* **69**, 245204 (2004).
- [94] S. Al Smairat and J. Graham, *J. Appl. Phys.* **130**, 125902 (2021).
- [95] R. Heid, B. Renker, H. Schober, P. Adelman, D. Ernst, and K.-P. Bohnen, *Phys. Rev. B* **67**, 180510 (2003).
- [96] C. Sevik, J. Bekaert, M. Petrov, and M. V. Milošević, *Phys. Rev. Mater.* **6**, 24803 (2022).
- [97] X.-L. Zhang and W.-M. Liu, *Sci. Rep.* **5**, 8964 (2015).
- [98] T. Shirasawa, M. Sugiki, T. Hirahara, M. Aitani, T. Shirai, S. Hasegawa, and T. Takahashi, *Phys. Rev. B* **89**, 195311 (2014).